

# The concept of event-size dependent exhaustion and its application to paraglacial rockslides

Stefan Hergarten<sup>1</sup>

<sup>1</sup>Institut für Geo- und Umwelt naturwissenschaften, Albert-Ludwigs-Universität Freiburg, Albertstr. 23B, 79104 Freiburg, Germany

**Correspondence:** Stefan Hergarten  
(stefan.hergarten@geologie.uni-freiburg.de)

**Abstract.** Rockslides are a major hazard in mountainous regions. In formerly glaciated regions, the disposition mainly arises from oversteepened topography and decreases through time. However, little is known about this decrease and thus about the present-day hazard of huge, potentially catastrophic rockslides. This paper presents a new theoretical concept that combines the decrease in disposition with the power-law distribution of rockslide volumes found in several studies. The concept starts

5 from a given initial set of potential events, which are randomly triggered through time at a probability that depends on event size. The developed theoretical framework is applied to paraglacial rockslides in the European Alps, where available data allow for constraining the parameters reasonably well. The results suggest that the probability of triggering increases roughly with the cube root of the volume. For small rockslides up to  $1000 \text{ m}^3$ , an exponential decrease of the frequency with an *e*-folding time longer than 65,000 yr is predicted. In turn, the predicted *e*-folding time is shorter than 2000 yr for volumes of  $10 \text{ km}^3$ , so  
10 that the occurrence of such huge rockslides is unlikely at present times. For the largest rockslide possible at present times, a median volume of 0.5 to  $1 \text{ km}^3$  is predicted. With a volume of  $0.27 \text{ km}^3$ , the artificially triggered rockslide that hit the Vajont reservoir in 1963, is thus not extraordinarily large. Concerning its frequency of occurrence, however, it can be considered a 700 to 1200-year event.

## 1 Introduction

15 Rockslides are a ubiquitous hazard in mountainous regions. The biggest rockslide in the European Alps since 1900 took place in 1963 at the Vajont reservoir. It involved a volume of about  $0.27 \text{ km}^3$ . Owing to an overtopping of the dam, it claimed more than 2000 lives. However, the reservoir played an important part in triggering this huge rockslide, so that it cannot be considered a natural event. The largest natural rockslides in the Alps since 1900 are considerably smaller (e.g., Gruner, 2006).

20 In turn, two huge rockslides with volumes of several cubic kilometers have been identified and dated. These are the Flims rockslide with a deposited volume of about  $10 \text{ km}^3$  (Aaron et al., 2020) in the carbonatic rocks of the Rhine valley and the Köfels rockslide with a deposited volume of about  $4 \text{ km}^3$  (Zangerl et al., 2021) in the crystalline rocks of the Oetz valley. Estimates of the ages of these two giant events scatter by some 100 years (Deplazes et al., 2007; Nicolussi et al., 2015, and references therein). Within this scatter, however, both ages are about 9500 BP. These ages refute the older idea of triggering by glacial debuttressing. Since the inner Alpine valleys were largely free of ice at about 18,000 BP (e.g., Ivy-Ochs et al., 2008),

25 an immediate relation to the deglaciation of the respective valleys can be excluded. Consequently, von Poschinger et al. (2006) concluded that rockslides of several cubic kilometers have to be taken into consideration also at present.

Although an immediate effect of deglaciation can be excluded for the Flims and Käfels rockslides, the former glaciation of the valleys plays a central part for rockslide disposition. In the context of paraglacial rock-slope failure, Cruden and Hu (1993) proposed the concept of exhaustion (see also Ballantyne, 2002a, b). The concept is similar to radioactive decay. Starting from 30 an initial population of potentially unstable sites, it is assumed that each of them is triggered at a given probability per time  $\lambda$ . Then both the remaining number of potentially unstable sites and the rockslide frequency decrease like  $e^{-\lambda t}$ . Analyzing a small data set of 67 rockslides with volumes  $V \geq 1000 \text{ m}^3$  ( $10^{-6} \text{ km}^3$ ) from the Canadian Rocky Mountains, where 14 similar potentially unstable sites were found, Cruden and Hu (1993) estimated  $\lambda = 0.18 \text{ kyr}^{-1}$ , equivalent to an e-folding time  $T = \lambda^{-1} = 5700 \text{ yr}$ .

35 As a main limitation, however, the estimate  $T = 5700 \text{ yr}$  refers to the total number of rockslides with  $V \geq 1000 \text{ m}^3$ . Whether this estimate could be transferred to rockslides of any given size is nontrivial. If this result could be transferred to rockslides of any size in the Alps, the present-day probability even of huge rockslides would be only by a factor of  $e^{\frac{9500}{5700}} \approx 5$  lower than it was at the time of the Flims and Käfels rockslides.

Analyzing the statistical distribution of landslide sizes became popular a few years later than the concept of exhaustion 40 was proposed, presumably pushed forward by the comprehensive analysis of several thousand landslides in Taiwan by Hovius et al. (1997). Reanalyzing several data sets, Malamud et al. (2004) found that landslides in unconsolidated material as well as rockfalls and rockslides follow a power-law distribution over some range in size. The exponent of the power law was found to be independent of the triggering mechanism (e.g., earthquakes, rainstorms or rapid snow melt), but is considerably lower for 45 rockfalls and rockslides than for landslides in unconsolidated material. The distinct dependence on the material was confirmed by Brunetti et al. (2009). For deeper insights into the scaling properties of landslides, the review article of Tebbens (2020) is recommended.

Several models addressing the power-law distribution of landslides were developed so far (Densmore et al., 1998; Hergarten and Neugebauer, 1998; Hergarten, 2012; Alvioli et al., 2014; Liucci et al., 2017; Jeandet et al., 2019; Campforts et al., 2020). Some of these studies discussed landslides in the context of self-organized criticality (SOC). The idea of SOC was introduced 50 by Bak et al. (1987) and promised to become a unifying theoretical concept for dynamic systems that generate events of various sizes following a power-law distribution. Jensen (1998) characterized SOC systems as slowly driven, interaction-dominated threshold systems. In the context of landslides, relief is generated directly or indirectly (e.g., in combination with fluvial incision) by tectonics. This process is rather continuous and slow. In turn, landslides take place as discrete events if a threshold is exceeded and consume relief. A system that exhibits SOC approaches some kind of long-term equilibrium between long-term 55 driving and instantaneous relaxation with power-law distributed event sizes.

Now the question arises how the idea of paraglacial exhaustion can be reconciled with the power-law distribution of rockslide sizes, perhaps in combination with SOC. While size distributions of rockfalls and rockslides were addressed in several studies during the previous decade (e.g., Bennett et al., 2012; Lari et al., 2014; Valagussa et al., 2014; Strunden et al., 2015; Tanyas et al., 2018; Hartmeyer et al., 2020; Mohadjer et al., 2020), only the two latest studies refer directly to paraglacial exhaustion.

60 Mohadjer et al. (2020) attempted to estimate the total volume of rockfalls in a deglaciated valley at different time scales up to 11,000 yr. In turn, Hartmeyer et al. (2020) investigated the rockfall activity at walls above a retreating glacier at much smaller spatial and temporal scales.

65 In this paper, a theoretical framework for event-size-dependent exhaustion is developed, which means that the decay constant  $\lambda$  depends on the event size. In the following section, it is illustrated that the Drossel-Schwabl forest-fire model as one of the simplest models in the field of SOC and the model for rockslide disposition proposed by Hergarten (2012) already predict such a behavior. In Sect. 3, the theoretical framework will be developed. This framework will be applied to the Alps in Sect. 4, and it will be investigated to what extent the sparse available data on large rockslides can be used to constrain the parameters.

## 2 Motivation

### 2.1 The Drossel-Schwabl forest-fire model

70 Let us start with the Drossel-Schwabl forest-fire model (DS-FFM in the following) as an example. While several in their spirit similar models were developed soon after the idea of SOC became popular, the version proposed by Drossel and Schwabl (1992) with a simplification introduced by Grassberger (1993) attracted the greatest interest. Although obviously oversimplified, it was found later that it reproduces some properties of real wildfires quite well (Malamud et al., 1998; Zinck and Grimm, 2008; Krenn and Hergarten, 2009).

75 The DS-FFM is a stochastic cellular automaton model that is usually considered on a two-dimensional square lattice with periodic boundary conditions. Each site can be either empty or occupied by a tree. In each time step, a given number  $\theta$  of new trees is planted at randomly selected sites, assuming that planting a tree at an already occupied site has no effect. Then a randomly selected site is ignited. If this site is occupied by a tree, this tree and the entire cluster of connected trees are burned. By default, only nearest-neighbor connections are considered.

80 Regardless of the initial condition, the DS-FFM self-organizes towards a quasi-steady state in which as many trees are burned as are planted on average. If the growth rate  $\theta$  and the size of the model are sufficiently large, about 40 % of all sites are occupied on average and the distribution of the fire sizes roughly follows a power law. The DS-FFM was investigated numerically and theoretically in numerous studies (e.g., Christensen et al., 1993; Henley, 1993; Clar et al., 1994; Pastor-Satorras and Vespignani, 2000; Pruessner and Jensen, 2002; Schenk et al., 2002; Hergarten and Krenn, 2011), resulting in a 85 more or less complete understanding of its properties.

Let us now assume that the growth of new trees ceases suddenly at some time in the quasi-steady state, so that the available clusters of trees are burned successively. Figure 1 shows an example computed on a small grid of  $256 \times 256$  sites with  $\theta = 100$ . It is immediately recognized that the largest fires take place quite early. This property is owing to the the mechanism of ignition. Each cluster of trees can be burned equivalently by igniting any of its trees. So the probability that a cluster of trees is burned is 90 proportional to the cluster size (number of trees). This implies that large clusters are preferred to small clusters at any time. This property was already used by Hergarten and Krenn (2011) for deriving a semi-phenomenological explanation of the power-law

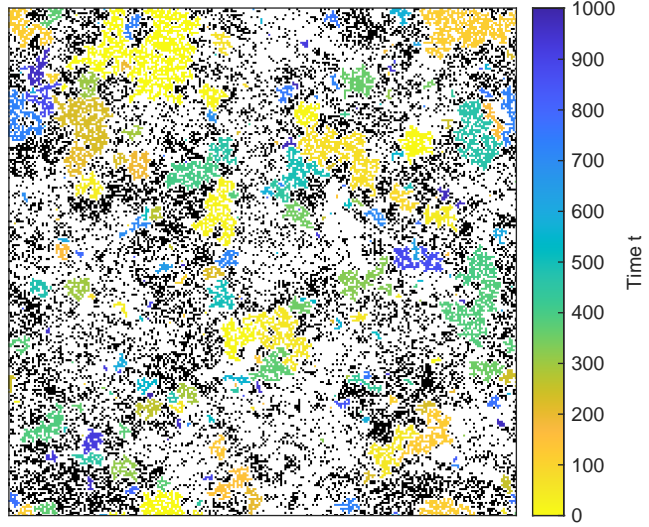


**Figure 1.** Burned clusters of trees without regrowth on a  $256 \times 256$  grid. One unit of time corresponds to one event of ignition. Colored patches correspond to clusters burned at different times. White sites were already empty in the beginning, while black clusters are still present after the simulated 1000 events of ignition.

distribution in the quasi-steady state and by Krenn and Hergarten (2009) for modifying the DS-FFM towards human-induced fires.

Owing to the preference of large fires, the DS-FFM in a phase without regrowth is an example of event-size dependent exhaustion. Figure 2 shows the size distribution of the fires derived from a simulation on a larger grid of  $65,536 \times 65,536$  sites with  $\theta = 10,000$ . It is immediately recognized that the distribution derived from the quasi-steady state (black curve) follows a power law only over a limited range. The rapid decline for  $s > 10^5$  is due to the finite growth rate  $\theta$ . As explained by Hergarten and Krenn (2011), the excess of fires at the transition to the rapid decline ( $s \approx 10^5$ ) is owing to the shape of large clusters and is thus a specific property of the DS-FFM, which is not relevant for the following considerations.

The distribution of the fires that take place during the first 10,000 steps after growth has ceased is almost identical to the distribution in the quasi-steady state. A small deficit is only visible at the tail. So the overall consumption of clusters during the first 10,000 steps is negligible, except for the largest clusters. The trend that large clusters are consumed more rapidly than small clusters is consolidated over larger time spans. As an example, the frequency of fires with sizes  $s \approx 10^5$  is in the time interval from  $t = 10^5$  to  $10^6$  by more than two decades lower than in the quasi-steady state, while the frequency of fires with  $s \lesssim 10^3$  is still almost unaffected.

As a central result, the power-law distribution of the fires is consumed through time from the tail. In particular, the exponent (slope in the double-logarithmic plot) stays the same in principle, while only the range of the power law becomes shorter. Finally, however, the decay also affects the frequency of the smallest fires.

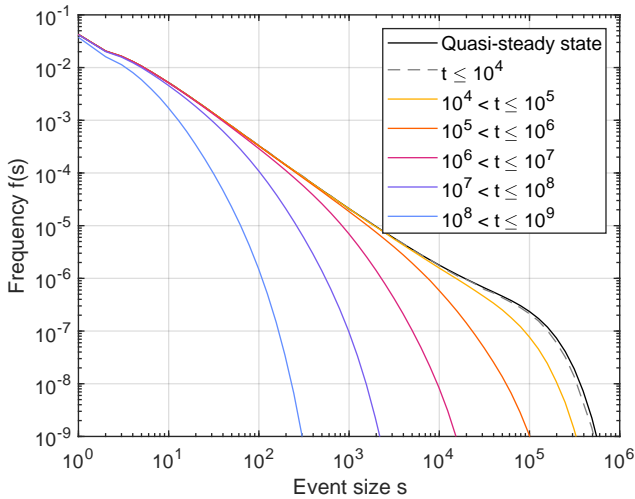


**Figure 2.** Frequency of the fires in the DS-FFM during phases without growing trees. All distributions were obtained from simulations on a  $65,536 \times 65,536$  grid with  $\theta = 10,000$  and smoothed by logarithmic binning with 10 bins per decade. The black curve describes the frequency of fires per ignition event in the quasi-steady state, while the other curves describe different time slices. These data were obtained by stacking 75 simulated sequences starting from different points of the quasi-steady state.

## 2.2 A simple model for rockslide disposition

110 Hergarten (2012) proposed a simple model for rockslide disposition. This model is based on topography alone and assumes that each site of a regular lattice may become unstable if exposed to a random trigger. The probability of failure  $p$  is assumed to be a function of the local slope  $S$ , measured in the direction of steepest descent among the 8 nearest and diagonal neighbors. Sites with a slope below a given slope  $S_{\min}$  always remain stable ( $p = 0$ ), while sites steeper than a given slope  $S_{\max}$  become unstable whenever exposed to a trigger ( $p = 1$ ). A linear increase in probability,

115 
$$p = \frac{S - S_{\min}}{S_{\max} - S_{\min}}, \quad (1)$$

is assumed in the range between  $S_{\min}$  and  $S_{\max}$ . As soon as a site becomes unstable, as much material as needed for reducing the slope to  $S_{\min}$  is removed, and a trigger is applied to all 8 neighbors. Depending on the topography, this may lead to large avalanches.

120 Applied to the topography of the Alps, the Himalayas, and the southern Rocky Mountains, the model reproduced the observed power-law distribution of rockslide volumes reasonably well. Differences between the considered mountain ranges were found concerning the transition from a power law to an exponential distribution at large volumes. However, the model has not been applied widely since then, except for the study on landslide dams by Argentin et al. (2021).

Figure 3 illustrates the application of the model to a region in Switzerland. Since the model has not been tested systematically for terrain models with less than 10 m grid spacing, the 2 m terrain model of Switzerland (Bundesamt für Landestopografie swisstopo, 2022) was resampled to 10 m grid spacing. Since the model is used only for illustration here, the parameter values

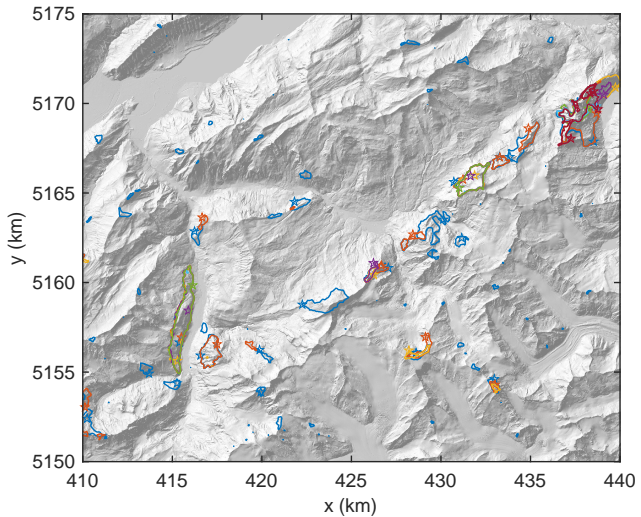


**Figure 3.** Simulated rockslide sites for a part of Switzerland. In addition to the outlines of the unstable areas, the respective triggering points are also shown for events with  $V \geq 10^{-4} \text{ km}^3 (10^5 \text{ m}^3)$ . Colors are just used for distinguishing overlapping outlines. Coordinates refer to UTM 32.

$S_{\min} = 1$  and  $S_{\max} = 5$  were adopted from Hergarten (2012) and Argentin et al. (2021). A total of 10 triggers per  $\text{km}^2$  was applied independently to the topography (so not a sequence of consecutive events).

As the main point to be illustrated, different triggering points result in very similar events at some locations. At some other locations, events arising from different triggers are overlapping, but differ in size. Both effects become stronger with increasing 130 event size. This means that larger potential rockslides are more likely triggered than smaller potential rockslides in the model.

Qualitatively, this behavior is similar to that of the DS-FFM, but more complex. Since randomness is not limited to triggering, but is also part of the propagation of instability, even rockslides of different sizes may be triggered from the same point. In contrast to the DS-FFM, finding a quantitative relation between event size and probability of being triggered is not trivial for the rockslide model.

135 It is, however, recognized that the triggering points are not distributed uniformly in the area, but are concentrated around the lower part of the outline. In this model, the initial instability preferably occurs at very steep sites and then predominantly propagates uphill since the uphill sites become steeper due to removing material. Accordingly, the increase in triggering probability with area (and thus also with volume) should be weaker than linear.

### 3 Theoretical framework

140 Let us assume that the process of exhaustion starts at  $t = 0$  from a given set of objects (potential events) described by a nondimensional size  $s$ . This size is defined in such a way that the probability  $\lambda$  of decay (generating an event) per time is

proportional to  $s$  (as in the DS-FFM),

$$\lambda(s) = \mu s, \quad (2)$$

with a given value  $\mu$ . Let  $\phi(s, t)$  be the frequency density of the objects still there at time  $t$ . Since  $\phi(s, t)$  refers to the number

145 of objects of size  $s$ , it decreases according to

$$\frac{\partial}{\partial t} \phi(s, t) = -\lambda(s) \phi(s, t) = -\mu s \phi(s, t). \quad (3)$$

This leads to

$$\phi(s, t) = \phi(s, 0) e^{-\mu s t}, \quad (4)$$

where  $\phi(s, 0)$  is the initial frequency density of the objects.

150 Let us further assume that the objects initially follow a power-law (Pareto) distribution, which is most conveniently written in the cumulative form

$$\Phi(s, 0) = n s^{-\alpha} \quad (5)$$

with an exponent  $\alpha$ . The cumulative frequency  $\Phi(s, t)$  describes the expected number of objects with sizes greater than or equal to  $s$  at time  $t$ . In the context of statistics,  $\Phi(s, t)$  is the complementary cumulative frequency, while the cumulative frequency

155 originally refers to the number of objects smaller than  $s$ . For a power-law distribution, considering the complementary frequency simplifies the equations and allows for a convenient graphical representation as a straight line in a double-logarithmic diagram.

Since  $\Phi(1, 0) = n$ , the initial number of objects with sizes  $s \geq 1$  is  $n$ . The respective frequency density is

$$\phi(s, 0) = -\frac{\partial}{\partial s} \Phi(s, 0) = n \alpha s^{-\alpha-1}, \quad (6)$$

160 which yields

$$\phi(s, t) = \phi(s, 0) e^{-\mu s t} = n \alpha s^{-\alpha-1} e^{-\mu s t} \quad (7)$$

in combination with Eq. (4).

Computing the cumulative frequency  $\Phi(s, t)$  requires the integration of Eq. (7):

$$\Phi(s, t) = \int_s^\infty \phi(\sigma, t) d\sigma = \int_s^\infty n \alpha \sigma^{-\alpha-1} e^{-\mu \sigma t} d\sigma. \quad (8)$$

165 Substituting  $u = \mu \sigma t$ , the integral can be transformed into

$$\Phi(s, t) = n \alpha (\mu t)^\alpha \int_{\mu s t}^\infty u^{-\alpha-1} e^{-u} du = n \alpha (\mu t)^\alpha \Gamma(-\alpha, \mu s t) \quad (9)$$

with the upper incomplete gamma function

$$\Gamma(q, x) = \int_x^\infty u^{q-1} e^{-u} du. \quad (10)$$

The negative rate of change in  $\phi(s, t)$  defines the frequency density of the events per unit time and at time  $t$ ,

$$170 \quad f(s, t) = -\frac{\partial}{\partial t} \phi(s, t) = \mu s \phi(s, t) = n \mu \alpha s^{-\alpha} e^{-\mu s t}. \quad (11)$$

The respective cumulative frequency of the events per unit time,  $F(s, t)$ , can be computed by performing the same steps as in Eqs. (8) and (9):

$$F(s, t) = \int_s^\infty f(\sigma, t) d\sigma = n \mu \alpha (\mu t)^{\alpha-1} \Gamma(1 - \alpha, \mu s t). \quad (12)$$

As an example, Fig. 4 shows the respective distributions for  $\alpha = 1.2$  (similar to the DS-FFM) and  $\mu = 1$  (which only affects the time scale). The two frequency densities  $f(s, t)$  and  $\phi(s, t)$  are still close to the respective initial densities at  $t = 10^{-3}$  over a considerable range of sizes. Their exponents differ by one ( $\alpha$  vs.  $\alpha + 1$ ). According to Eqs. (4) and (11), the actual frequency density drops below the respective power law by a factor of  $e$  at a size

$$175 \quad s_c = \frac{1}{\mu t}. \quad (13)$$

Owing to this property,  $s_c$  can be used for characterizing the transition from a power law to an exponential decrease at large event sizes. In this example,  $s_c = 1000$  at  $t = 10^{-3}$ .

For the cumulative frequencies, the deviations from the respective power law extend towards smaller sizes compared to the frequency densities. The stronger deviation arises from the dependence of the cumulative frequency at size  $s$  on the frequency density of all greater sizes.

#### 4 Application to paraglacial rockslides in the Alps

185 Applying the framework developed in Sect. 3 to paraglacial rockslides in a given region requires the definition of the event size  $s$  in the sense of Eq. (2) at first. This means that the probability of failure at a potential rockslide site is proportional to  $s$ . As discussed in Sect. 2.2, defining  $s$  is not straightforward here. So let us assume a general power-law relation

$$190 \quad s = \left( \frac{V}{V_0} \right)^\gamma \quad (14)$$

with a given exponent  $\gamma$  and a reference volume  $V_0$ . Since  $\mu$  in Eq. (2) is the decay constant  $\lambda$  for  $s = 1$ , it is the decay constant for rockslides with a volume  $V = V_0$  here, and  $n$  (Eq. 5) is the initial number of potential rockslide sites with  $V \geq V_0$ .

If the shape of the detached body was independent of its volume, areas would be proportional to  $V^{\frac{2}{3}}$  and lengths proportional to  $V^{\frac{1}{3}}$ . So assuming that failure can be initiated at each point of the fracture surface at the same probability would lead to

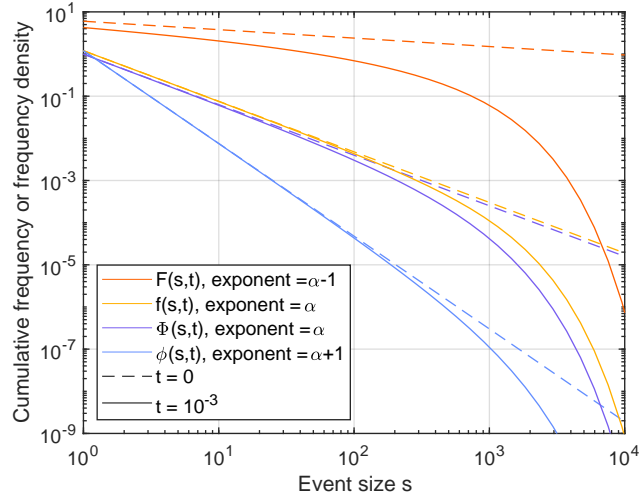


**Figure 4.** Cumulative frequency and frequency density of the events per unit time ( $F(s,t)$ ,  $f(s,t)$ ) and the objects still present ( $\Phi(s,t)$ ,  $\phi(s,t)$ ) at  $t = 0$  and  $t = 10^{-3}$  for  $\alpha = 1.2$  and  $\mu = 1$ . All distributions were normalized to the total number  $n$  of objects with sizes  $s \geq 1$  ( $n = 1$  in all equations).

$\gamma = \frac{2}{3}$ . Taking into account that large detached bodies are relatively thinner than small bodies (Larsen et al., 2010) would result in  $\gamma > \frac{2}{3}$ , but still considerably below 1. The simple model considered in Sect. 2.2 suggests that the length of the outcrop line might be the relevant property rather than the area, which would result in  $\gamma \approx \frac{1}{3}$ .

Keeping the exponent  $\gamma$  as an unknown parameter, forward modeling based on the concept of size-dependent exhaustion involves the four parameters  $\gamma$ ,  $\mu$ ,  $\alpha$ , and  $n$ . When referring to real-world data, however, it is not known when the process of exhaustion started. Therefore, a real-world time  $t_0$  must be assigned to the starting point  $t = 0$  used in the theoretical framework, which introduces an additional parameter.

Since data on the frequency of rockslides are sparse and the completeness of inventories is often an issue, validating the exhaustion model and constraining its parameters is challenging. For the European Alps as a whole, a combination of historical and prehistorical data is used in the following.

1. 18 rockslides with volumes between 0.001 and 0.01 km<sup>3</sup> (1 to 10 million m<sup>3</sup>) took place from 1850 to 2020 CE. These are 15 events until 2000 CE reported by Gruner (2006) and 3 events in the 21<sup>th</sup> century (Dents du Midi, 2006; Bondo 2011 and 2017).
2. 7 rockslides with volumes between 0.01 and 0.1 km<sup>3</sup> (10 to 100 million m<sup>3</sup>) took place from 1850 to 2020 CE (Gruner, 2006).
3. 2 rockslides with volumes greater than 0.1 km<sup>3</sup> took place from 1000 to 2020 CE (Gruner, 2006).
4. At  $t = 9450$  BP, the largest potential rockslide volume is 10 km<sup>3</sup>, corresponding to age (Deplazes et al., 2007) and volume (Aaron et al., 2020) of the Flims rockslide.

5. At  $t = 9500$  BP, the second-largest potential rockslide volume is  $4 \text{ km}^3$ , corresponding to age (Nicolussi et al., 2015) and volume (Zangerl et al., 2021) of the Kofels rockslide.

6. At  $t = 3210$  BP, the largest potential rockslide volume is  $1.1 \text{ km}^3$ , corresponding to the Kandersteg rockslide (Singeisen et al., 2020).

215 7. At  $t = 4150$  BP, the second-largest potential rockslide volume is  $1 \text{ km}^3$ , corresponding to the Fernpass rockslide (Gruner, 2006).

Anthropogenically triggered rockslides were not taken into account in these data.

The data 4–7 differ from the data 1–3 since they are not inventories over a given time span, but refer to the largest or second-largest available volumes at a given time. The respective statistical distributions are described by rank-ordering statistics (e.g., 220 Sornette, 2000, Chapter 6). Despite the different types of the data, they can be combined in a maximum likelihood formalism. The likelihood of a given parameter combination ( $\gamma$ ,  $\mu$ ,  $\alpha$ ,  $n$ , and  $t_0$ ) is the product of seven factors then. The first three factors are the probabilities that 18, 5, and 2 events occur in the volume ranges and time spans defined in the criteria 1–3. The fourth factor is the probability density of the volume of the largest potential rockslide at  $V = 10 \text{ km}^3$  and  $t = 9450$  BP. The remaining factors are obtained from the same principle. The respective expressions for the seven factors are developed in Appendix A.

225 However, the 7 constraints defined above provide a very limited basis for constraining the 5 parameters  $\gamma$ ,  $\mu$ ,  $\alpha$ ,  $n$ , and  $t_0$ . Since these constraints refer to volumes  $V \geq 10^{-3} \text{ km}^3$  (1 million  $\text{m}^3$ ), it would be useful to include information about smaller events from local inventories. As exhaustion predominantly affects the frequency of large events, it makes sense to assume that the power-law distribution typically found in local inventories defines the initial distribution, so that the initial frequency density  $f(s, 0)$  of the events follows a power law with the exponent  $\alpha$  (Eq. 11). As reviewed by Brunetti et al. 230 (2009), this exponent is typically in the range  $\alpha_V \in [1.1, 1.4]$ , where the subscript V indicates that this value refers to volume instead of the generic measure of event size  $s$ . The relation between  $\alpha_V$  and  $\alpha$  is easily obtained from the cumulative frequency of the events at  $t = 0$ ,

$$F(s, 0) \propto s^{-(\alpha-1)} \propto V^{-\gamma(\alpha-1)} = V^{-(\alpha_V-1)} \quad (15)$$

with

235  $\alpha_V = \gamma(\alpha - 1) + 1$ . (16)

While  $\alpha_V$  is used instead of  $\alpha$  in the following, knowledge about  $\alpha_V$  from real-world inventories is not directly included in the maximum likelihood approach. The typical range  $\alpha_V \in [1.1, 1.4]$  is only used for checking whether the estimate obtained from the maximum likelihood approach is consistent with local inventories.

240 Technically, all computations were performed in terms of  $s$  (Eq. 14) instead of  $V$  and consequently using  $\alpha$  instead of  $\alpha_V$ . The transfer to  $V$  and  $\alpha_V$ , which are more useful than  $s$  and  $\alpha$  in the interpretation, was performed afterwards.

Figure 5a shows the likelihood as a function of the exponents  $\alpha_V$  and  $\gamma$ . For each combination of these two parameters, the respective values of  $\mu$ ,  $n$ , and  $t_0$  that maximize the likelihood were computed. Since absolute values of the likelihood have no

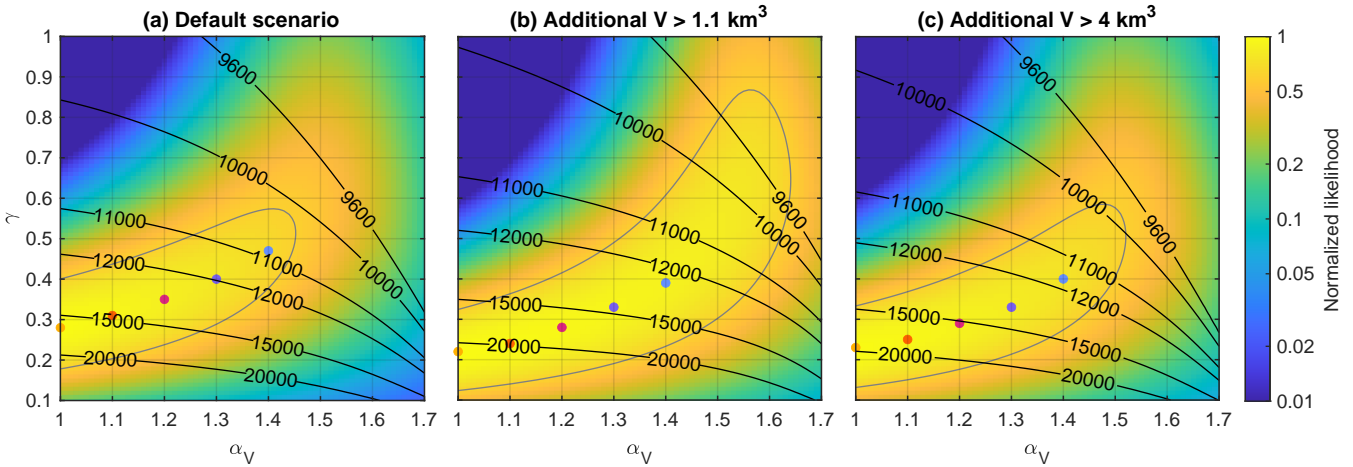


**Figure 5.** Likelihood as a function of  $\alpha_V$  and  $\gamma$  for different scenarios. The maximum likelihood values taken over all combinations of the remaining parameters  $\mu$ ,  $n$ , and  $t_0$  are shown. Likelihood values are normalized to the maximum value, and the gray contour line refers to  $e^{-0.5} \approx 0.61$  of the maximum likelihood. Black contour lines describe the obtained time  $t_0$  (BP) at which the process of exhaustion started. Colored dots refer to the points with the highest likelihood for  $\alpha_V = 1, 1.1, 1.2, 1.3$  and  $1.4$ .

immediate meaning, all values are normalized to the maximum values. In addition to the likelihood values, the obtained values of  $t_0$  are illustrated in form of contour lines, while the obtained values of  $\mu$  and  $n$  are not shown.

245 The highest likelihood is even achieved for  $\alpha_V = 1$  in combination with  $\gamma = 0.28$ . However, the likelihood decreases only by a factor of 0.68 for  $\alpha_V = 1.4$  and  $\gamma = 0.47$ . For a Gaussian likelihood function, the standard deviation would correspond to a reduction by a factor of  $e^{-0.5} \approx 0.61$ , which is marked by the gray contour line. So the entire parameter region inside the gray line cannot be considered unlikely.

Qualitatively, however, the observed increase in likelihood towards smaller exponents  $\alpha_V$  makes sense. Since size-dependent 250 exhaustion particularly reduces the frequency of large events, it may introduce a bias towards larger estimates of  $\alpha_V$  in rockslide inventories compared to the initial distribution. As illustrated in Fig. 4, the deviation from the power law increases continuously with increasing event size, so that there is no distinct range of validity for the power-law distributions. As a consequence, any method that does not take into account the deviation from the power law explicitly will likely overestimate the exponent. So the real value of  $\alpha_V$  may be rather at the lower edge of the observed interval  $\alpha_V \in [1.1, 1.4]$  or even be slightly below 1.1.

255 The data set used for calibration is not only quite small, but also potentially incomplete. For the inventories used for constraints 1 and 2, incompleteness should not be a serious problem. The inventory used for the third constraint is small and thus does not contribute much information, so that an additional event would not change much. In turn, the assumptions on the largest or second-largest potential rockslide at a given time are more critical. As an example, the Kandersteg rockslide was assumed to be much older ( $t = 9600$  BP, Tinner et al., 2005) than the recent estimate ( $t = 3210$  BP, Singeisen et al., 2020) for 260 several years. So the criteria 6 and 7 would have been different a few years ago.

In general, constraints 4–7 based on rank ordering may be affected by the discovery of unknown huge rockslides as well as by new estimates of ages or volumes of rockslides that are already known. Perhaps even more important, rockslides larger than those in constraints 4–7 may take place in the future.

To illustrate the effect of a potential incompleteness, it is assumed that the Kandersteg rockslide is not the largest potential event at  $t = 3210$  BP, but that there is one additional larger event. For the formalism, it makes no difference whether this event already took place or will take place in the future. As a moderate scenario, it is assumed that this additional event is smaller than the Köfels rockslide ( $1.1 \text{ km}^3 < V < 4 \text{ km}^3$ ). This scenario shifts the rank of the events in constraints 6 and 7 by one (Kandersteg to second and Fernpass to third).

As shown in Fig. 5b, this scenario shifts the likely range towards lower values of the exponent  $\gamma$ . According to its definition (Eq. 14), lower values of  $\gamma$  correspond to a weaker dependence of the decay constant on volume. So the exhaustion of large events becomes relatively slower then, which is the expected behavior if we assume an additional large event at a late time.

The third scenario (Fig. 5c) goes a further step ahead by assuming that there was a potential event even larger than the Köfels rockslide, but smaller than the Flims rockslide ( $4 \text{ km}^3 < V < 10 \text{ km}^3$ ) at the time of the Kandersteg rockslide. This means that the rank of the Köfels rockslide in constraint 5 changes from second to third. However, the likelihood values shown in Fig. 5c reveal no further shift towards lower values of  $\gamma$ , but even a small tendency back towards the default scenario (Fig. 5a).

In the following, the rockslide size distributions corresponding to the five dots in all three scenarios (Fig. 5a–c) are considered. This means that the values  $\alpha_V = 1, 1.1, 1.2, 1.3$ , and  $1.4$  are considered for each scenario, while only the most likely values of the other parameters  $\gamma, \mu, n$ , and  $t_0$  are used.

Let us now come back to the question about the size of the largest rockslide to be expected in the future in the Alps, so for the largest potential rockslide volume at present (2020 CE). Let  $\Phi(V, t)$  be the cumulative frequency at present time (Eq. 9 expressed in terms of  $V$  instead of  $s$ ). Then  $\Phi(V_0, t)$  is the total number of potential rockslides with  $V \geq V_0$ . Each of them is smaller than  $V$  at a probability  $1 - \frac{\Phi(V, t)}{\Phi(V_0, t)}$ . Raising this probability to the power of  $\Phi(V_0, t)$  yields the probability that all potential rockslides are smaller than  $V$ . Then

$$P(V, t) = 1 - \left(1 - \frac{\Phi(V, t)}{\Phi(V_0, t)}\right)^{\Phi(V_0, t)} \quad (17)$$

is the probability that the largest potential rockslide has a volume of at least  $V$ . Using the relation  $(1 - \frac{x}{n})^n \rightarrow e^{-x}$  for  $n \rightarrow \infty$ , this probability can be approximated by

$$P(V, t) = 1 - e^{-\Phi(V, t)} \quad (18)$$

if the total number  $\Phi(V_0, t)$  is sufficiently large.

Figure 6 shows the cumulative probability  $P(V, t)$  of the largest potential rockslide volume at present (2020 CE). For the default scenario, this volume is greater than 0.5 to 0.7  $\text{km}^3$  (depending on  $\alpha_V$ ) at 50 % probability (the median). This variation in the median size is owing to the finding that different values of the exponent  $\alpha_V$  yield similar values of the likelihood, so that  $\alpha_V$  cannot be constrained further from the data.

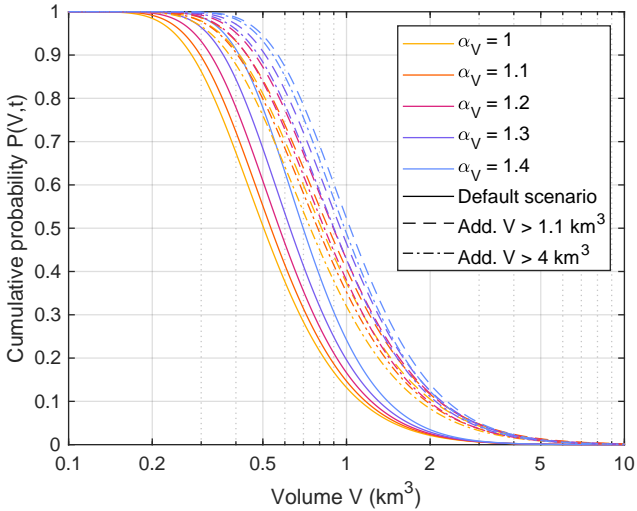


**Figure 6.** Cumulative probability of the largest rockslide at present (2020 CE). Different line types refer to the three considered scenarios.

As already expected from Fig. 5b,c, the two scenarios with an additional large rockslide are similar. However, the median of the largest available volume is in the range between  $0.74 \text{ km}^3$  and  $1.04 \text{ km}^3$  and thus about 1.5 times higher than for the 295 default scenario. So the estimate of the largest volume to be expected involves two sources of uncertainty with the same order of magnitude. First, there is the inability to constrain  $\alpha_V$  sufficiently well, owing to the limited amount of data. Second, there is the potential incompleteness of the data concerning the largest events at a given time, which is here taken into account by considering the two alternative scenarios.

If we go back to the time of the Kandersteg rockslide ( $t = 3210 \text{ BP}$ ), the relevance of the uncertainties changes. As shown 300 in Fig. 7, the volumes predicted for the considered values of  $\alpha_V$  differ only by about 10 %. At that time, the statistics of the largest possible rockslides are still constrained well by the criteria 4–7. The predictions obtained for different values of  $\alpha_V$  start to spread when proceeding towards the recent time. In turn, the difference between the scenarios stays roughly the same. So the question whether the Kandersteg rockslide was the largest potential event at its time or only the second-largest has a similar effect at its time as it has today.

305 As a third source of uncertainty, the statistical nature of the prediction must be taken into account. Depending on  $\alpha_V$  and on the considered scenario, the present-day 85 % and 15 % quantiles are  $0.3\text{--}0.65 \text{ km}^3$  and  $0.95\text{--}2 \text{ km}^3$ , respectively (Fig. 6). So the 70 % probability range (comparable to the standard deviation of a Gaussian distribution) of the largest potential rockslide covers a factor of about 3 in volume. This uncertainty is even larger than the two other contributions to the uncertainty. It is an inherent property of the statistical distribution and would not decrease even if all parameter values ( $\gamma$ ,  $\mu$ ,  $\alpha_V$ ,  $n$ , and  $t_0$ ) were 310 known exactly.

In all scenarios, the probability that a rockslide with  $V \geq 3 \text{ km}^3$  takes place in the future is below 5 %. The probability of a rockslide with  $V \geq 10 \text{ km}^3$  is even lower than 0.2 %. These results shed new light on the conclusion of von Poschinger et al. (2006) that rockslides of several cubic kilometers have to be taken into consideration also at present. Such events may

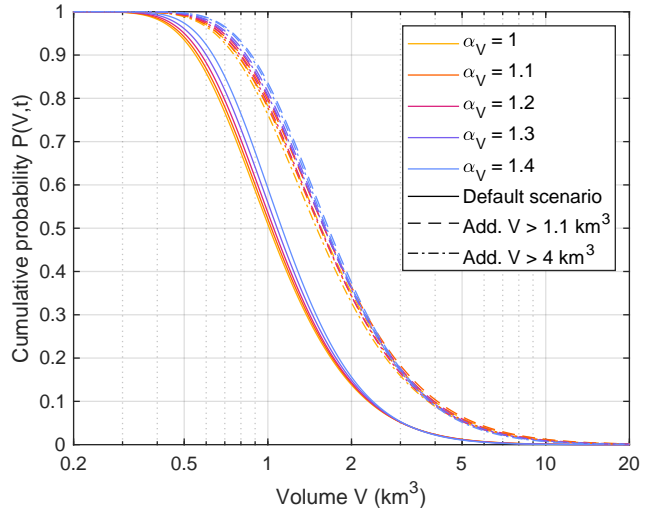


**Figure 7.** Cumulative probability of the largest rockslide at the time of the Kandersteg rockslide (3210 BP). Different line types refer to the three considered scenarios.

be possible concerning their mechanism and the climatic conditions, but it is very unlikely that such an event would still be  
315 waiting to take place according to this framework.

In turn, the probability that there will be no rockslide with  $V \geq 0.24 \text{ km}^3$  is also less than 5 % ( $P = 0.95$  in Fig. 6). This result sheds new light on the artificially triggered rockslide that stroke the Vajont reservoir in 1963 and claimed about 2000 lives. With a volume of about  $0.27 \text{ km}^3$ , this rockslide cannot be considered extraordinarily large, and natural events of this size must be taken into account in the future.

320 Figure 8 brings the probability of occurrence into play. It shows the expected cumulative frequency  $F(V,t)$  (events per year) at present. All curves are strikingly close to each other for  $5 \times 10^{-4} \text{ km}^3 \leq V \leq 0.02 \text{ km}^3$ . In this range, the frequencies are constrained well by recent inventories (constraints 1 and 2).

325 The 100-year event ( $F(V,t) = 0.01 \text{ yr}^{-1}$ ) has a volume of  $0.04\text{--}0.045 \text{ km}^3$ . This is approximately the size of the rockslide which took place in Val Pola in 1987 (e.g. Crosta et al., 2003). In the context of large events, the 475-year event is often considered, which is the event with a probability of 10 % over 50 years. The predicted volume of this event is  $0.15\text{--}0.2 \text{ km}^3$ . The predicted frequency of the size of the Vajont rockslide ( $V = 0.27 \text{ km}^3$ ) is between than  $0.00145 \text{ yr}^{-1}$  and  $0.00085 \text{ yr}^{-1}$ , which means that a 700 to 1200-year event was triggered at the reservoir in 1963. Finally, rockslides with a volume of  $1 \text{ km}^3$  should be expected at a probability of less than 1 per 5000 years.

330 Let us now come back to the question of what we can learn about the process of exhaustion. Concerning the process, the exponent  $\gamma$  is the central parameter, while  $\alpha_V$  does not refer immediately to exhaustion and  $\mu$ ,  $n$ , and  $t_0$  should depend on the considered case study. The likelihood plots shown in Fig. 5 tentatively suggest  $\gamma \approx \frac{1}{3}$ . Despite the uncertainty of this estimate,  $\gamma \approx \frac{1}{3}$  is clearly more likely than  $\gamma \approx \frac{2}{3}$ . In terms of triggering a given site from different points, this finding suggests that

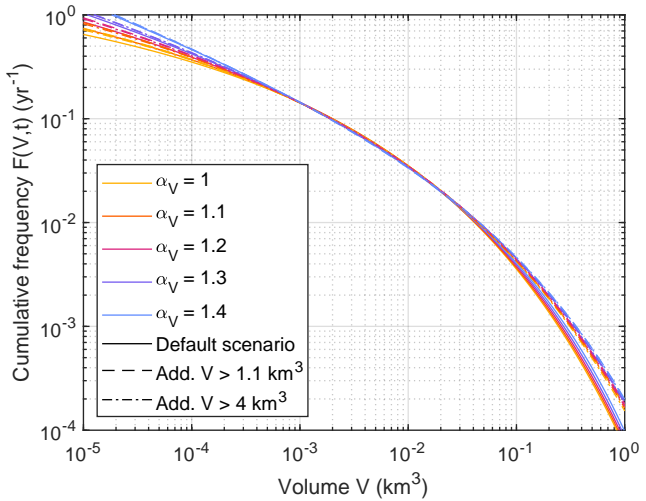


**Figure 8.** Cumulative rockslide frequency at present (2020 CE). Different line types refer to the three considered scenarios.

triggering should rather take place from the outcrop line of the failure surface (or a part of it) than from any point of the entire failure surface.

335 This knowledge may also be useful for validating or refuting models. So far, reproducing an exponent in the range  $\alpha_V \in [1.1, 1.4]$  seems to be the main goal of models of rockslide disposition. Although already challenging, this is still a rather weak criterion. In the context of SOC, it would only refer to the quasi-steady state, while the exponent  $\gamma$  provides additional information about the behavior if driving ceases.

340 However, the simulation shown in Sect. 2.2 already revealed that determining  $\gamma$  from simulations may be challenging. The observed concentration of the triggering points around the outlines of the predicted rockslides tentatively suggests that the model proposed by Hergarten (2012) may behave correctly, but the occurrence of overlapping events of different sizes make a direct analysis difficult. Simulating and analyzing exhaustion starting from a quasi-steady state would be an alternative strategy of validation for comprehensive models that also include long-term driving, such as HyLands (Campforts et al., 2020).

As a fundamental property of the process of exhaustion, Fig. 9 shows the *e*-folding time

$$345 \quad T = \frac{1}{\lambda} = \frac{1}{\mu s} = \frac{1}{\mu} \left( \frac{V}{V_0} \right)^{-\gamma}. \quad (19)$$

For  $V \geq 10 \text{ km}^3$ ,  $T$  is shorter than 2000 yr for all scenarios. In turn,  $T > 65,000 \text{ yr}$  for  $V \leq 10^{-6} \text{ km}^3$  ( $1000 \text{ m}^3$ ). So paraglacial exhaustion should have a minor effect on the frequency of events with  $V \leq 1000 \text{ m}^3$ . The *e*-folding time  $T = 5700 \text{ yr}$  estimated by Cruden and Hu (1993) occurs in Fig. 9 in a range from  $V = 0.04 \text{ km}^3$  to  $V = 0.5 \text{ km}^3$ , depending on the considered scenario. However, Cruden and Hu (1993) found  $T = 5700 \text{ yr}$  as a lumped *e*-folding time for an inventory 350 with  $10^{-6} \text{ km}^3 \leq V \leq 0.05 \text{ km}^3$ . So it seems that Cruden and Hu (1993) overestimated the exhaustion of small rockslides (underestimated  $T$ ), perhaps due to undetected potential landslide sites.

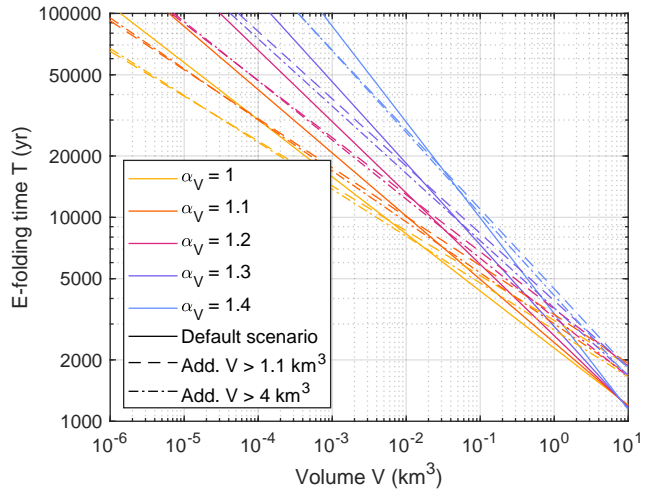


**Figure 9.**  $e$ -folding time of the exhaustion as a function of the volume. Different line types refer to the three considered scenarios.

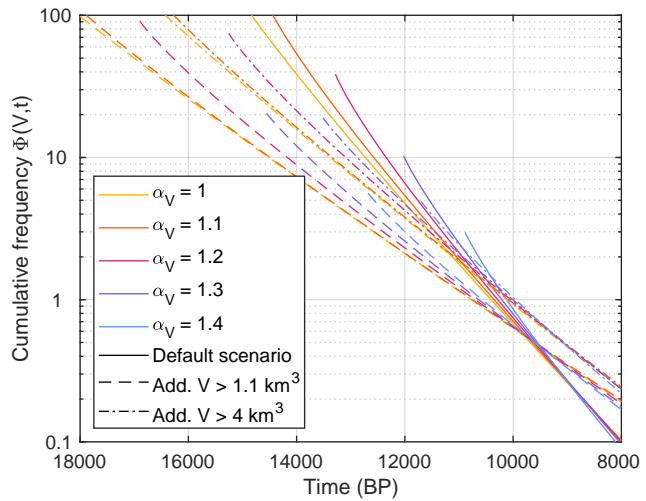


**Figure 10.** Cumulative frequency of potential rockslide sites with  $V \geq 10 \text{ km}^3$ . Different line types refer to the three considered scenarios.

From a geological point of view, the time  $t_0$  at which the process of exhaustion started might even be the most interesting parameter. As shown in Fig. 5, the likely parameter range even comprises values of  $t_0$  earlier than 15000 BP. Such values would bring the deglaciation of the major valleys back into play. However, Fig. 10 reveals that the results become unrealistic between 355  $t_0$  and the time of the Flims rockslide (9450 BP). In particular for small values of  $\alpha_V$ , the approach predicts an unrealistically large number of rockslides with  $V \geq 10 \text{ km}^3$  during the early phase of exhaustion. All combinations that yield a starting time  $t_0$  earlier than 15000 BP predict more than 10 potential rockslides with  $V \geq 10 \text{ km}^3$  at  $t = 15000 \text{ BP}$ , and it is very unlikely that the Flims rockslide is the only preserved one among those.

However,  $t_0$  is only a hypothetic time at which exhaustion started from a power-law distribution without any cutoff at large sizes. As observed in Sect. 2.1, even the quasi-steady state of the DS-FFM already shows a cutoff in the power-law distribution at large event sizes. This behavior is typical for models in the context of SOC. While the cutoff can be attributed to the finite growth rate in the DS-FFM, it is even not clear what the quasi-steady state would look like in the rockslide model discussed in Sect. 2.2. For the paraglacial exhaustion process it is, however, obvious that the initial relief imposes an upper limit to the potential rockslide volumes. So the process already must start from a power-law distribution with a cutoff. At least qualitatively, it makes sense to assume that it starts from the distribution including some exhaustion at a time later than  $t_0$  (formally,  $\Phi(V, t)$  for  $t > 0$ ). A later starting time would correspond to a lower initial relief then. In order to estimate how much later than  $t_0$  the process started, we can make the hypothesis that there were not many paraglacial rockslides with  $V \geq 10 \text{ km}^3$  in total, which means that  $\Phi(V, t)$  should not be much larger than 1 for  $V = 10 \text{ km}^3$  at the time when the process of exhaustion started. If we assume  $1 \leq \Phi(V, t) \leq 2$ , the process of exhaustion should have started between 12000 BP and 10000 BP for all scenarios in Fig. 10.

In view of this result, the deglaciation of the major valleys cannot only be refuted as an immediate trigger of the huge paraglacial landslides in the Alps, but also as the start of the process of exhaustion. The starting point may, however, be the massive degradation of permafrost caused by rapid warming in the early Holocene era. For the Kofels rockslide, the potential relation to the degradation of permafrost was discussed by Nicolussi et al. (2015) and Zangerl et al. (2021). In these studies, the 2000-year timespan from the beginning of the Holocene era to the rockslide was considered too long for a direct triggering. However, the concept of exhaustion only assumes that the respective sites became potentially unstable when permafrost retreated. Returning to Fig. 9, the predicted  $e$ -folding times are between 1100 and 2600 years for volumes from 4 to  $10 \text{ km}^3$ . In view of this result, a time span of 2000 yr to the occurrence of an actual instability is not too long.

However, the question for the actual trigger for the respective rockslides remains open. In principle, even the question whether a unique trigger is needed is still open. Large instabilities may also develop slowly (e.g., Riva et al., 2018; Spreafico et al., 2021) and failure may finally occur without a unique trigger.

## 5 Conclusions

In this study, a theoretical concept for event-size dependent exhaustion was developed. The process starts from a given set of potential events, which are randomly triggered through time. In contrast to a previous approach (Cruden and Hu, 1993), the probability of triggering depends on event size.

The concept was applied to paraglacial rockslides in the European Alps. Since available inventories cover only a quite short time span and older data are limited to a few huge rockslides, constraining the parameters involves a large uncertainty. Nevertheless, some fundamental results could be obtained.

Assuming that the probability of triggering is related to the volume  $V$  by a power law  $V^\gamma$ , the results indicate exponents  $\gamma \approx \frac{1}{3}$  or even slightly lower. Interpreting the dependence on volume as the possibility to initiate an event from different points, this result suggests that initiation may rather start from the outcrop line of the failure surface (or from a part of this line) than

from any point of the failure surface. The exponent  $\gamma$  may be helpful for validating or refuting statistical or process-based models.

The concept of event-size dependent exhaustion predicts an exponential decrease of rockslide frequency through time with a decay constant depending on  $V$ . For small rockslides with  $V \leq 1000 \text{ m}^3$ , the respective  $e$ -folding time is longer than 65,000 yr. So the frequency of small rockslides should not have decreased much since the last glaciation. In turn, the predicted  $e$ -folding time is shorter than 2000 yr for  $V \geq 10 \text{ km}^3$ . So the occurrence of rockslides in the order of magnitude of the Flims rockslide is unlikely at present times. These  $e$ -folding times are, however, consistent with the idea that the process of exhaustion was initiated by the degradation of permafrost at the beginning of the Holocene epoch.

For the largest rockslide possible at present times, different considered scenarios predict a median volume of 0.5 to 1  $\text{km}^3$ . However, the predicted frequency of such large events is low (less than 1 per 5000 years for  $V \geq 1 \text{ km}^3$ ). The predicted 100-year event has a volume of 0.04–0.045  $\text{km}^3$ . The artificially triggered rockslide at the Vajont reservoir (1963 CE,  $V = 0.27 \text{ km}^3$ ) can be considered a 700 to 1200-year event in this context.

*Code and data availability.* All codes are available in a Zenodo repository at <https://doi.org/10.5281/zenodo.7313868> (Hergarten, 2022).

This repository also contains the data obtained from the computations. The author is happy to assist interested readers in reproducing the results and performing subsequent research.

## Appendix A: The maximum likelihood formalism

In this section, a maximum likelihood approach that combines data of the two types discussed in Sect. 4 is developed.

The first type of data (constraints 1–3 in Sect. 4) refers to the number of events in a given range of sizes  $[s_1, s_2]$  during a given time interval  $[t_1, t_2]$ . The expected number  $N$  is easily obtained from the cumulative frequency  $\Phi(s, t)$  of the potential events (Eq. 9) as

$$N = \Phi(s_1, t_1) - \Phi(s_2, t_1) - \Phi(s_1, t_2) + \Phi(s_2, t_2). \quad (\text{A1})$$

Then the respective factor in the likelihood is the probability that the actual number  $n$  of events occurs, which is given by the Poisson distribution

$$L_{1-3} = \frac{N^n}{n!} e^{-N}. \quad (\text{A2})$$

The second type of data (constraints 4–7 in Sect. 4) is described by rank-ordering statistics. The probability density of the  $k^{\text{th}}$  largest among  $n$  events is

$$p_k(s) = \binom{n}{k} \left(1 - \int_s^\infty p(\sigma) d\sigma\right)^{n-k} \binom{k}{1} p(s) \left(\int_s^\infty p(\sigma) d\sigma\right)^{k-1} \quad (\text{A3})$$

(Sornette, 2000, Eq. 6.4), where  $p(s)$  is the probability density of the events. Replacing  $p(s)$  by the frequency density  $\phi(s) = 420 np(s)$ , switching to the cumulative frequency  $\Phi(s)$ , and joining the binomial coefficients yields

$$p_k(s) = \frac{(n-1)!}{(n-k)!(k-1)!} \left(1 - \frac{\Phi(s)}{n}\right)^{n-k} \phi(s) \left(\frac{\Phi(s)}{n}\right)^{k-1}. \quad (\text{A4})$$

In the limit  $n \rightarrow \infty$  at finite  $k$ , terms  $n-1, \dots, n-k$  can be replaced by  $n$ . In combination with the relation  $\left(1 - \frac{x}{n}\right)^n \rightarrow e^x$ , we obtain

$$p_k(s) = \frac{1}{(k-1)!} e^{-\Phi(s)} \Phi(s)^{k-1} \phi(s). \quad (\text{A5})$$

425 If  $s$  was the measured property, the probability density  $p_k(s)$  would already be the respective factor of the likelihood. Here, however,  $V$  is the measured property, so that the likelihood is obtained by transforming  $p_k(s)$  from  $s$  to  $V$  according to

$$L_{4-7} = p_k(s) \frac{ds}{dV} \quad (\text{A6})$$

with

$$\frac{ds}{dV} = V_0^{-\gamma} \gamma V^{\gamma-1} = \frac{\gamma}{V_0} s^{\frac{\gamma-1}{\gamma}} \quad (\text{A7})$$

430 obtained from Eq. (14). Then the likelihood is

$$L_{4-7} = \frac{1}{(k-1)!} e^{-\Phi(s)} \Phi(s)^{k-1} \phi(s) \frac{\gamma}{V_0} s^{\frac{\gamma-1}{\gamma}}. \quad (\text{A8})$$

Finally, the total likelihood is the product of the seven factors according to Eqs. (A2) and Eq. (A8).

*Competing interests.* The author declares that there is no conflict of interest.

*Acknowledgements.* The author would like to thank Maria Teresa Brunetti and an anonymous reviewer for their constructive comments and 435 Oded Katz for the editorial handling.

## References

Aaron, J., Wolter, A., Loew, S., and Volken, S.: Understanding failure and runout mechanisms of the Flims rockslide/rock avalanche, *Front. Earth Sci.*, 8, 224, <https://doi.org/10.3389/feart.2020.00224>, 2020.

Alvioli, M., Guzzetti, F., and Rossi, M.: Scaling properties of rainfall induced landslides predicted by a physically based model, *Geomorphology*, 213, 38–47, <https://doi.org/10.1016/j.geomorph.2013.12.039>, 2014.

Argentin, A.-L., Robl, J., Prasicek, G., Hergarten, S., Hölbling, D., Abad, L., and Dabiri, Z.: Controls on the formation and size of potential landslide dams and dammed lakes in the Austrian Alps, *Nat. Hazards Earth Syst. Sci.*, 21, 1615–1637, <https://doi.org/10.5194/nhess-21-1615-2021>, 2021.

Bak, P., Tang, C., and Wiesenfeld, K.: Self-organized criticality. An explanation of 1/f noise, *Phys. Rev. Lett.*, 59, 381–384, <https://doi.org/10.1103/PhysRevLett.59.381>, 1987.

Ballantyne, C. K.: A general model of paraglacial landscape response, *Holocene*, 12, 371–376, <https://doi.org/10.1191/0959683602hl553fa>, 2002a.

Ballantyne, C. K.: Paraglacial geomorphology, *Quat. Sci. Rev.*, 21, 1935–2017, [https://doi.org/10.1016/S0277-3791\(02\)00005-7](https://doi.org/10.1016/S0277-3791(02)00005-7), 2002b.

Bennett, G. L., Molnar, P., Eisenbeiss, H., and McArdell, B. W.: Erosional power in the Swiss Alps: characterization of slope failure in the 450 Illgraben, *Earth Surf. Process. Landforms*, 37, 1627–1640, <https://doi.org/10.1002/esp.3263>, 2012.

Brunetti, M. T., Guzzetti, F., and Rossi, M.: Probability distribution of landslide volumes, *Nonlin. Processes Geophys.*, 16, 179–188, <https://doi.org/10.5194/npg-16-179-2009>, 2009.

Bundesamt für Landestopografie swisstopo: swissALTI3D DTM 2m, <https://www.swisstopo.admin.ch/de/geodata/height/alti3d.html>, last access: 17.05.2023, 2022.

455 Campforts, B., Shobe, C. M., Steer, P., Vanmaercke, M., Lague, D., and Braun, J.: HyLands 1.0: a hybrid landscape evolution model to simulate the impact of landslides and landslide-derived sediment on landscape evolution, *Geosci. Model Dev.*, 13, 3863–3886, <https://doi.org/10.5194/gmd-13-3863-2020>, 2020.

Christensen, K., Flyvbjerg, H., and Olami, Z.: Self-organized critical forest-fire model: mean-field theory and simulation results in 1 to 6 dimensions, *Phys. Rev. Lett.*, 71, 2737–2740, <https://doi.org/10.1103/PhysRevLett.71.2737>, 1993.

460 Clar, S., Drossel, B., and Schwabl, F.: Scaling laws and simulation results for the self-organized critical forest-fire model, *Phys. Rev. E*, 50, 1009–1018, <https://doi.org/10.1103/PhysRevE.50.1009>, 1994.

Crosta, G. B., Imposimato, S., and Roddeman, D. G.: Numerical modelling of large landslides stability and runout, *Nat. Hazards Earth Syst. Sci.*, 3, 523–538, <https://doi.org/10.5194/nhess-3-523-2003>, 2003.

Cruden, D. M. and Hu, X. Q.: Exhaustion and steady state models for predicting landslide hazards in the Canadian Rocky Mountains, 465 *Geomorphology*, 8, 279–285, [https://doi.org/10.1016/0169-555X\(93\)90024-V](https://doi.org/10.1016/0169-555X(93)90024-V), 1993.

Densmore, A. L., Ellis, M. A., and Anderson, R. S.: Landsliding and the evolution of normal-fault-bounded mountains, *J. Geophys. Res.*, 103, 15 203–15 219, <https://doi.org/10.1029/98JB00510>, 1998.

Deplazes, G., Anselmetti, F. S., and Hajdas, I.: Lake sediments deposited on the Flims rockslide mass: the key to date the largest mass movement of the Alps, *Terra Nova*, 19, 252–258, <https://doi.org/10.1111/j.1365-3121.2007.00743.x>, 2007.

470 Drossel, B. and Schwabl, F.: Self-organized critical forest-fire model, *Phys. Rev. Lett.*, 69, 1629–1632, <https://doi.org/10.1103/PhysRevLett.69.1629>, 1992.

Grassberger, P.: On a self-organized critical forest fire model, *J. Phys. A*, 26, 2081–2089, <https://doi.org/10.1088/0305-4470/26/9/007>, 1993.

Gruner, U.: Bergstürze und Klima in den Alpen – gibt es Zusammenhänge?, *Bull. angew. Geol.*, 11, 25–34, <https://doi.org/10.5169/seals-226166>, 2006.

475 Hartmeyer, I., Delleske, R., Keuschnig, M., Krautblatter, M., Lang, A., Schrott, L., and Otto, J.-C.: Current glacier recession causes significant rockfall increase: the immediate paraglacial response of deglaciating cirque walls, *Earth Surf. Dynam.*, 8, 729–751, <https://doi.org/10.5194/esurf-8-729-2020>, 2020.

Henley, C. L.: Statics of a “self-organized” percolation model, *Phys. Rev. Lett.*, 71, 2741–2744, <https://doi.org/10.1103/PhysRevLett.71.2741>, 1993.

480 Hergarten, S.: Topography-based modeling of large rockfalls and application to hazard assessment, *Geophys. Res. Lett.*, 39, L13402, <https://doi.org/10.1029/2012GL052090>, 2012.

Hergarten, S.: Event-size dependent exhaustion and paraglacial rockslides, <https://doi.org/10.5281/zenodo.7313868>, 2022.

Hergarten, S. and Krenn, R.: A semi-phenomenological approach to explain the event-size distribution of the Drossel-Schwabl forest-fire model, *Nonlin. Processes Geophys.*, 18, 381–388, <https://doi.org/10.5194/npg-18-381-2011>, 2011.

485 Hergarten, S. and Neugebauer, H. J.: Self-organized criticality in a landslide model, *Geophys. Res. Lett.*, 25, 801–804, <https://doi.org/10.1029/98GL50419>, 1998.

Hovius, N., Stark, C. P., and Allen, P. A.: Sediment flux from a mountain belt derived by landslide mapping, *Geology*, 25, 231–234, [https://doi.org/10.1130/0091-7613\(1997\)025<0231:SFFAMB>2.3.CO;2](https://doi.org/10.1130/0091-7613(1997)025<0231:SFFAMB>2.3.CO;2), 1997.

Ivy-Ochs, S., Kerschner, H., Reuther, A., Preusser, F., Heine, K., Maisch, M., Kubik, P. W., and Schlüchter, C.: Chronology of the last glacial 490 cycle in the European Alps, *J. Quaternary Sci.*, 23, 559–573, <https://doi.org/10.1002/jqs.1202>, 2008.

Jeandet, L., Steer, P., Lague, D., and Davy, P.: Coulomb mechanics and relief constraints explain landslide size distribution, *Geophys. Res. Lett.*, 46, 4258–4266, <https://doi.org/10.1029/2019GL082351>, 2019.

Jensen, H. J.: *Self-Organized Criticality – Emergent Complex Behaviour in Physical and Biological Systems*, Cambridge University Press, Cambridge, New York, Melbourne, 1998.

495 Krenn, R. and Hergarten, S.: Cellular automaton modelling of lightning-induced and man made forest fires, *Nat. Hazards Earth Syst. Sci.*, 9, 1743–48, <https://doi.org/10.5194/nhess-9-1743-2009>, 2009.

Lari, S., Frattini, P., and Crosta, G. B.: A probabilistic approach for landslide hazard analysis, *Engin. Geol.*, 182, 3–14, <https://doi.org/10.1016/j.enggeo.2014.07.015>, 2014.

Larsen, I. J., Montgomery, D. R., and Korup, O.: Landslide erosion controlled by hillslope material, *Nature Geosci.*, 3, 247–251, 500 <https://doi.org/10.1038/ngeo776>, 2010.

Liucci, L., Melelli, L., Suteanu, C., and Ponziani, F.: The role of topography in the scaling distribution of landslide areas: A cellular automata modeling approach, *Geomorphology*, 290, 236–249, <https://doi.org/10.1016/j.geomorph.2017.04.017>, 2017.

Malamud, B. D., Morein, G., and Turcotte, D. L.: Forest fires: an example of self-organized critical behavior, *Science*, 281, 1840–1842, <https://doi.org/10.1126/science.281.5384.1840>, 1998.

505 Malamud, B. D., Turcotte, D. L., Guzzetti, F., and Reichenbach, P.: Landslide inventories and their statistical properties, *Earth Surf. Process. Landforms*, 29, 687–711, <https://doi.org/10.1002/esp.1064>, 2004.

Mohadjer, S., Ehlers, T. A., Nettlesheim, M., Ott, M. B., Glotzbach, C., and Drews, R.: Temporal variations in rockfall and rock-wall retreat rates in a deglaciated valley over the past 11 ky, *Geology*, 48, 594–598, <https://doi.org/10.1130/G47092.1>, 2020.

Nicolussi, K., Spötl, C., Thurner, A., and Reimer, P. J.: Precise radiocarbon dating of the giant Kofels landslide (Eastern Alps, Austria), 510 *Geomorphology*, 243, 87–91, <https://doi.org/10.1016/j.geomorph.2015.05.001>, 2015.

Pastor-Satorras, R. and Vespignani, A.: Corrections to scaling in the forest-fire model, *Phys. Rev. E*, 61, 4854–4859, <https://doi.org/10.1103/physreve.61.4854>, 2000.

Pruessner, G. and Jensen, H. J.: Broken scaling in the forest-fire model, *Phys. Rev. E*, 65, 056707, <https://doi.org/10.1103/PhysRevE.65.056707>, 2002.

515 Riva, F., Agliardi, F., Amitrano, D., and Crosta, G. B.: Damage-based time-dependent modeling of paraglacial to postglacial progressive failure of large rock slopes, *J. Geophys. Res. Earth Surf.*, 123, 124–141, <https://doi.org/10.1002/2017JF004423>, 2018.

Schenk, K., Drossel, B., and Schwabl, F.: Self-organized critical forest-fire model on large scales, *Phys. Rev. E*, 65, 026135, <https://doi.org/10.1103/PhysRevE.65.026135>, 2002.

Singeisen, C., Ivy-Ochs, S., Wolter, A., Steinemann, O., Akçar, N., Yesilyurt, S., and Vockenhuber, C.: The Kandersteg rock avalanche (Switzerland): integrated analysis of a late Holocene catastrophic event, *Landslides*, 17, 1297–1317, <https://doi.org/10.1007/s10346-020-01365-y>, 2020.

520 Sornette, D.: *Critical Phenomena in Natural Sciences – Chaos, Fractals, Selforganization and Disorder: Concepts and Tools*, Springer, Berlin, Heidelberg, New York, 2000.

Spreafico, M. C., Sternai, P., and Agliardi, F.: Paraglacial rock-slope deformations: sudden or delayed response? Insights from an integrated 525 numerical modelling approach, *Landslides*, 18, 1311–1326, <https://doi.org/10.1007/s10346-020-01560-x>, 2021.

Strunden, J., Ehlers, T. A., Brehm, D., and Nettesheim, M.: Spatial and temporal variations in rockfall determined from TLS measurements in a deglaciated valley, Switzerland, *J. Geophys. Res. Earth Surf.*, 120, 1251–1273, <https://doi.org/10.1002/2014JF003274>, 2015.

Tanyas, H., Allstadt, K. E., and van Westen, C. J.: An updated method for estimating landslide-event magnitude, *Earth Surf. Process. Landforms*, 43, 1836–1847, <https://doi.org/10.1002/esp.4359>, 2018.

530 Tebbens, S. F.: Landslide scaling: A review, *Earth Space Sci.*, 7, e2019EA000662, <https://doi.org/10.1029/2019EA000662>, 2020.

Tinner, W., Kaltenrieder, P., Soom, M., Zwahlen, P., Schmidhalter, M., Boschetti, A., and Schlüchter, C.: Der nacheiszeitliche Bergsturz im Kandertal (Schweiz): Alter und Auswirkungen auf die damalige Umwelt, *Eclogae geol. Helv.*, 98, 83–95, <https://doi.org/10.1007/s00015-005-1147-8>, 2005.

535 Valagussa, A., Frattini, P., and Crosta, G. B.: Earthquake-induced rockfall hazard zoning, *Engin. Geol.*, 182, 213–225, <https://doi.org/10.1016/j.enggeo.2014.07.009>, 2014.

von Poschinger, A., Wassmer, P., and Maisch, M.: The Flims rockslide: history of interpretation and new insights, in: *Landslides from Massive Rock Slope Failure*, edited by Evans, S. G., Scarascia-Mugnozza, G., Strom, A., and Hermanns, R. L., pp. 329–356, Springer, Dordrecht, [https://doi.org/10.1007/978-1-4020-4037-5\\_18](https://doi.org/10.1007/978-1-4020-4037-5_18), 2006.

Zangerl, C., Schneeberger, A., Steiner, G., and Mergili, M.: Geographic-information-system-based topographic reconstruction and 540 geomechanical modelling of the Köfels rockslide, *Nat. Hazards Earth Syst. Sci.*, 21, 2461–2483, <https://doi.org/10.5194/nhess-21-2461-2021>, 2021.

Zinck, R. D. and Grimm, V.: More realistic than anticipated: A classical forest-fire model from statistical physics captures real fire shapes, *Open Ecol. J.*, 1, 8–13, <https://doi.org/10.2174/1874213000801010008>, 2008.